

Supplementary Information

Clay-based anion-selective 2D nanofluidics boost natural osmotic power generation

Linhan Xie, Shiwen Wang, Jiadong Tang, Yiqi Jing, Yuhong Jin, Jingbing Liu, Hao Wang, Qianqian Zhang*

*Corresponding author. Email: zhangqianqian@bjut.edu.cn

Contents

Section S1. Supplementary notes

Section S2. Supplementary Figures and tables

Fig. S1. SEM and EDS images of CoAl-CO₃²⁻ LDH.

Fig. S2. XRD and FT-IR images of LDH.

Fig. S3. Dispersion and Particle size distribution of LDH nanosheets.

Fig. S4. Variation of ionic conductance with temperature in 2D-NFM and Bulk solution.

Fig. S5. V_{os} and I_{os} of 2D-NFM in different concentration gradients of KCl solutions.

Fig. S6. Initiation and Termination diffusion sites of K⁺ and Cl⁻ ions in DFT model.

Fig. S7. Schematic of the model for COMSOL simulation.

Fig. S8. Simulation results of ion concentration distribution in multichannel nanofluidic systems.

Fig. S9. I-T curves of 2D-NFM in artificial seawater/river water for prolonged operation without electrolyte supplementation.

Fig. S10. Current densities of 2D-NFM with different thicknesses.

Fig. S11. Physical photos of 2D-NFM for 15 days of continuous operation.

Fig. S12. I-V curves of 2D-NFM for 15 days of continuous operation.

Fig. S13. Current densities and Output power densities of 2D-NFM at different test areas.

Fig. S14. Current densities and Output power densities of 2D-NFM in NaCl solution with different concentration gradients.

Fig. S15. Current and Output power densities of 2D-NFM at different temperatures.

Fig. S16. Current densities and Output power densities of 2D-NFM at high salinity solution.

Fig. S17. Current densities and Output power densities of 2D-NFM at NaCl solution containing dyes and biological protein.

Fig. S18. Current densities and Output power densities of 2D-NFM at different pH.

Fig. S19. Zeta potential of 2D-NFM at different pH.

Fig. S20. Models of the interaction between different anions and 2D-NFM.

Fig. S21. Photo of osmotic energy harvesting device based on 2D-NFM.

Table S1. Results of ICP-AES analysis of CoAl-CO₃²⁻ LDH.

Table S2. Performance comparison of anion-selective membranes.

Table S3. The major anion and cation concentrations (M) in seawater.

References

Supplementary Notes

Supplementary Note 1 | Calculation of LDH crystal layer spacing and 2D-NFM layer spacing

The layer spacing of LDH crystal and 2D-NFM can be calculated according to the Bragg equation [1]:

$$2d\sin\theta = n\lambda \quad (S1)$$

where d is the layer spacing, θ is the angle between the incident wave and the scattering plane, λ is the wavelength (~ 0.154 nm) of the incident wave and $n=1$. The XRD image shows that the characteristic peaks of the (003) and (006) crystal planes of CoAl-CO_3^{2-} LDH appear at 11.76° and 23.62° , corresponding to crystal plane spacings of 0.752 nm and 0.376 nm, respectively. The characteristic peaks of the (003) and (006) crystal planes of CoAl-Cl^- LDH appear at 11.63° and 23.28° , corresponding to crystal plane spacings of 0.760 nm and 0.382 nm. The XRD image of 2D-NFM shows the characteristic peak at 7.11° , corresponding to a layer spacing of 1.06 nm. After 48 h of immersion in water, the layer spacing is enlarged to 1.24 nm due to swelling of the membrane.

Supplementary Note 2 | Calculation for surface charge density of 2D-NFM

The surface charge density (σ) of 2D-NFM in electrolytes of different concentrations can be calculated using the Grahame equation [2]:

$$\sigma = \frac{\varepsilon_0 \varepsilon_r \zeta}{\lambda_d} \quad (S2)$$

where ε_0 is the vacuum dielectric constant, ε_r is the dielectric constant of water, ζ is the zeta potential of 2D-NFM. λ_d is the Debye shielding length, which can be calculated according to formula [3]:

$$\lambda_d = \sqrt{\frac{\varepsilon_0 \varepsilon_r K_B T}{2n_{\text{bulk}} z^2 e^2}} \quad (S3)$$

where K_B is the Boltzmann constant, T is the absolute temperature, n_{bulk} is the concentration of the bulk solution, z is the valence state of the ions in the electrolyte and e is the electron constant. It can be seen that the higher the concentration of the bulk solution, the smaller the Debye shielding length.

Supplementary Note 3 | Calculation for ionic migration activation energy of 2D-NFM and bulk solution

The ionic migration activation energy of 2D-NFM and bulk solution can be

calculated according to the Arrhenius equation [4]:

$$G = G_0 e^{-\frac{E_a}{RT}} \quad (\text{S4})$$

where G is the ion conductance, G_0 is the Arrhenius constant, E_a represents ionic migration activation energy, R is the ideal gas constant and T is the absolute temperature.

Supplementary Note 4 | COMSOL simulation

The ion transport behavior in 2D-NFM nano-channels has been simulated using commercial finite-element software COMSOL Multiphysics 5.6 [5, 6]. The numerical simulations were performed based on the coupled Poisson and Nernst-Planck equations (PNP) equations by setting appropriate boundary parameters. The ion transport behavior within the charged nano-channels can be described by the NP equation, which is defined as the flux of each ion:

$$j_i = -D_i(\nabla c_i + \frac{z_i F c_i}{RT} \nabla \phi) \quad (\text{S5})$$

where j_i , D_i , c_i , z_i , and ϕ are the ionic flux, diffusion coefficient, ion concentration, valence number for each species i and electrical potential, respectively. F , R and T is Faraday constant, universal gas constant and Kelvin temperature.

The relationship between electrical potential and ion concentration can be defined by the Poisson equation:

$$\nabla^2 \phi = -\frac{F}{\varepsilon} \sum z_i c_i \quad (\text{S6})$$

The electrostatic boundary condition is given by:

$$-n \cdot \nabla \phi = \frac{\sigma_s}{\varepsilon_0 \varepsilon_r} \quad (\text{S7})$$

where n is the unit normal vector to the wall surface and σ is the surface charge density of the walls. ε_0 , ε_r are the permittivity of a vacuum, the permittivity of water.

Usually, the system is simplified under steady state conditions, and when the system reaches a steady state, the ion fluxes should satisfy a time-independent continuity equation:

$$\nabla \cdot j_i = 0 \quad (\text{S8})$$

Finally, the ion concentration distribution is solved by using the finite element method coupled PNP equations under the given geometric conditions and appropriate boundary conditions.

Furthermore, a simplified model of nanochannel and electrolyte chamber is constructed (Fig. S7). The length of the nanochannel is set to 1000 nm and the pore size is set to 10 nm (The pore size is not set according to the actual pore size of the nanochannel of 1.06 nm, because too small a pore size will lead to severe polarization during the simulation). The channel size and length of the model of multichannel nanofluidic system are the same as single-channel nanofluidic system model, except that the number of nanochannels in the multichannel nanofluidic system is increased. The electrolyte chamber is set to be 400 nm long and 200 nm wide (The chamber is also simplified model and do not based on the dimensions of an actual electrochemical chamber). Then, 10 mM KCl solution is used as the electrolyte and the surface charge density of the nanochannels is set to be 5.71 mC/m², which is consistent with the experimental test data.

Supplementary Note 5 | Theoretical calculations based on DFT

The Theoretical calculations based on DFT are calculated by the CP2K software. The GGA-PBE functional [7] is used to describe the electron exchange correlation of the system, and the Goedecker-Teter-Hutter pseudopotential is used to treat the inner electrons and nuclei of the atoms. The basis group of all atoms is the DZVP-MOLOPT basis group. The truncation energy of the Gaussian mixed plane wave used for the theoretical calculations is 400 Ry, and the Brillouin zone integration of the LDH is performed on a 2*8*2 K-grid. During the transition state search, the CI-NEB algorithm [8] is used to calculate ion diffusion paths with eight interpolation points. In the calculation process of interaction energy, $E_{\text{Interaction energy}} = E_{\text{total}} - E_{\text{LDH}} - E_{\text{ions}}$.

During the calculation process of ionic diffusion barrier, a model for the diffusion of K⁺ and Cl⁻ ions in nanochannels of 2D-NFM is first constructed, in which the atomic ratio of Co and Al is 2:1. Then, by structural optimization of different adsorption positions of K⁺ and Cl⁻ ions in the model, the most stable adsorption sites are selected as the initiation and termination sites for the diffusion (Fig. S6). Eventually, the diffusion barriers of K⁺ and Cl⁻ ions from the initiation site to the termination site are calculated by DFT.

Supplementary Figures and Tables

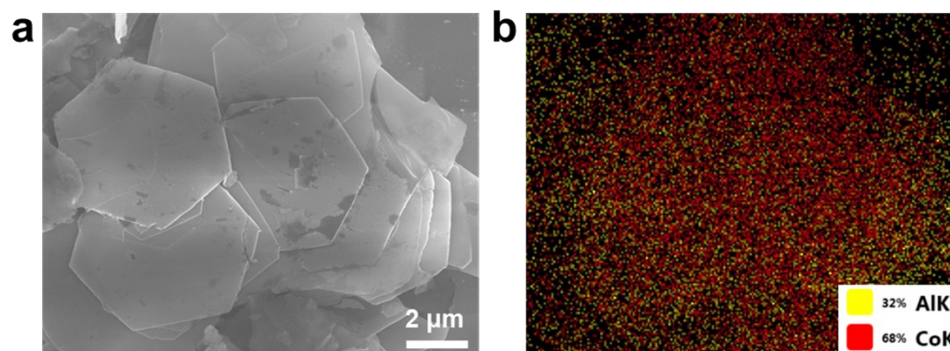


Fig. S1 (a) SEM and (b) EDS images of CoAl-CO₃²⁻ LDH.

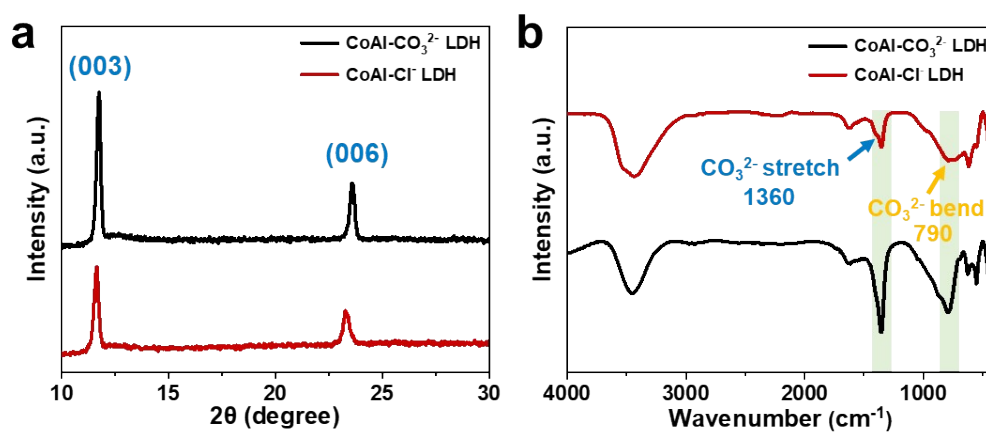


Fig. S2 (a) XRD and (b) FT-IR images of LDH.

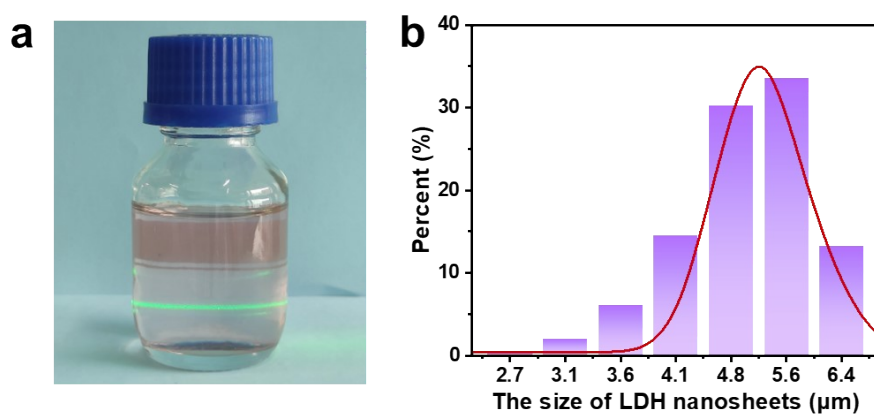


Fig. S3 (a) Dispersion and (b) Particle size distribution of LDH nanosheets.

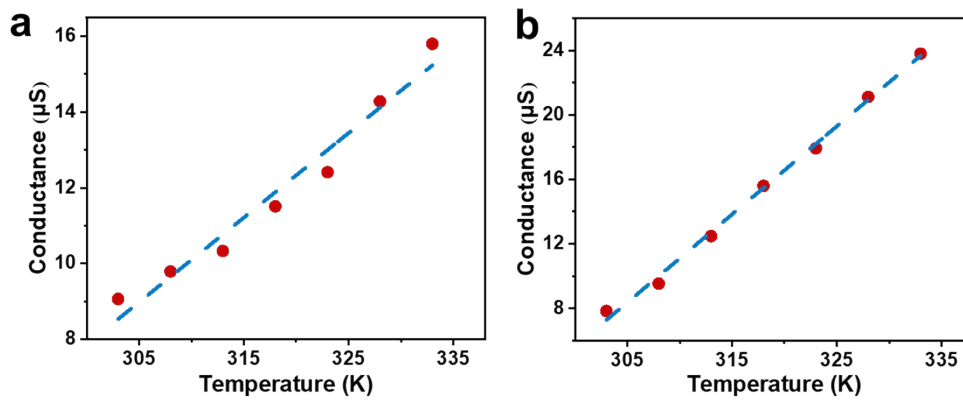


Fig. S4 Variation of ionic conductance with temperature in (a) 2D-NFM and (b) Bulk solution.

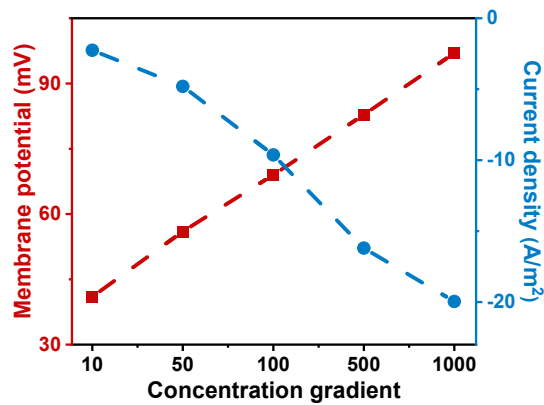


Fig. S5 V_{os} and I_{os} of 2D-NFM in different concentration gradients of KCl solutions.

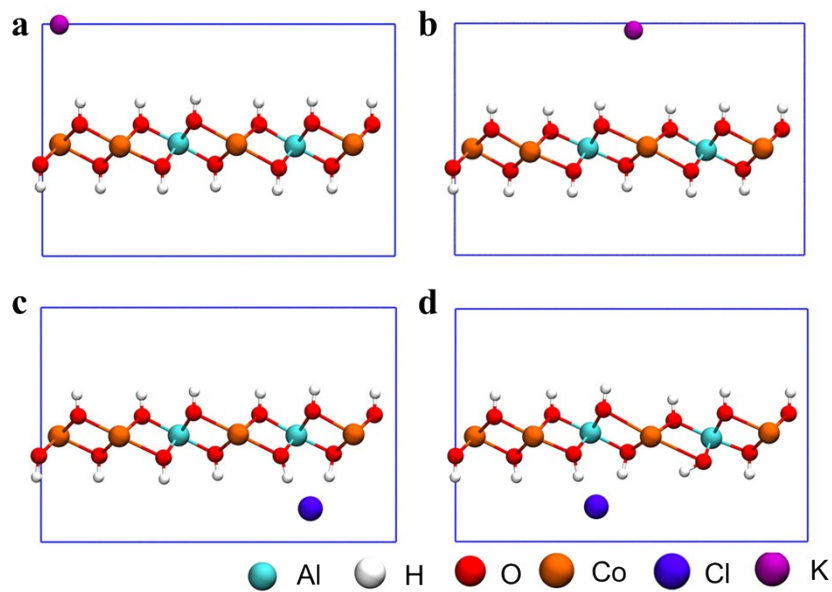


Fig. S6 (a) Initiation and (b) Termination diffusion sites of K⁺ ion in DFT model. (c) Initiation and (d) Termination diffusion sites of Cl⁻ ion in DFT model.

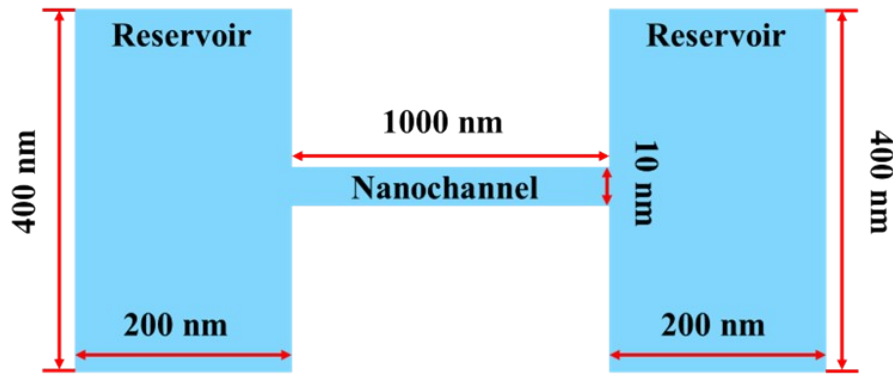


Fig. S7 Schematic of the model for COMSOL simulation.

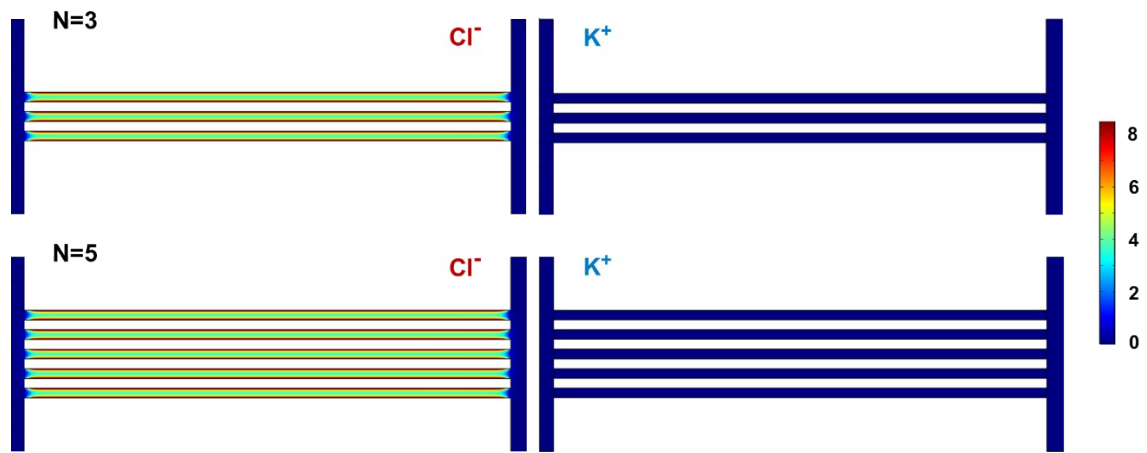


Fig. S8 Simulation results of ion concentration distribution in multichannel nanofluidic systems.

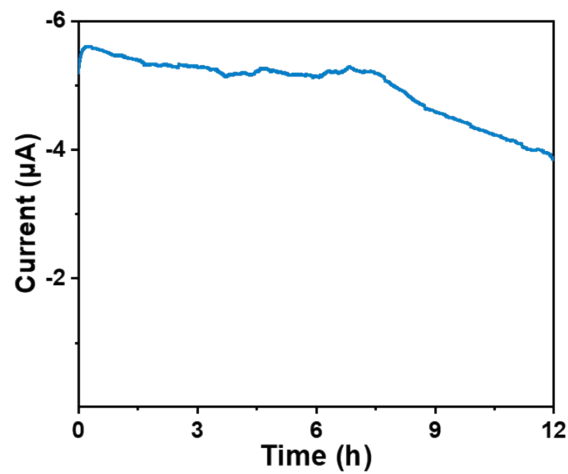


Fig. S9 I-T curves of 2D-NFM in artificial seawater/river water for prolonged operation without electrolyte refreshing.

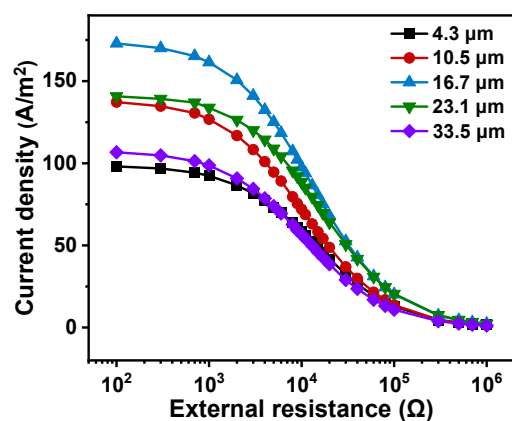


Fig. S10 Current densities of 2D-NFM with different thicknesses in NaCl solution with 50-fold concentration gradient.

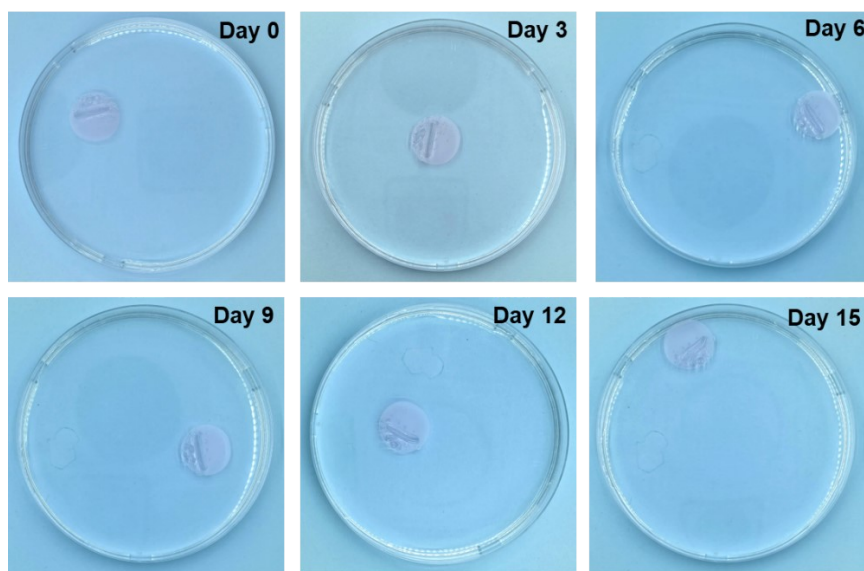


Fig. S11 Physical photos of 2D-NFM for 15 days of continuous operation.

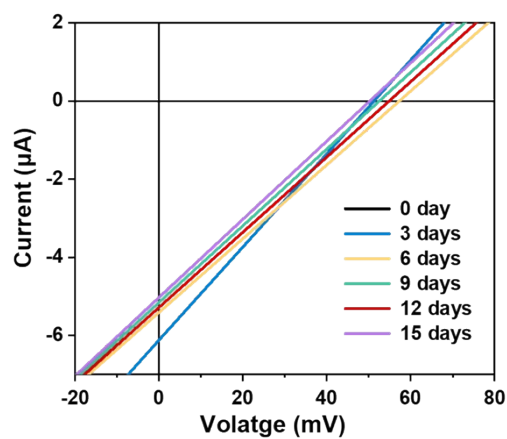


Fig. S12 I-V curves of 2D-NFM for 15 days of continuous operation.

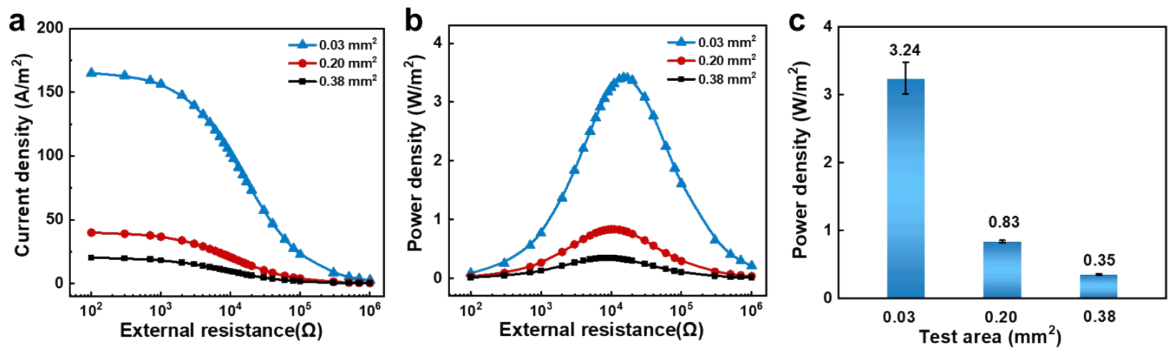


Fig. S13 (a) Current densities and (b, c) Output power densities of 2D-NFM at different test areas (0.01 M/0.5 M NaCl).

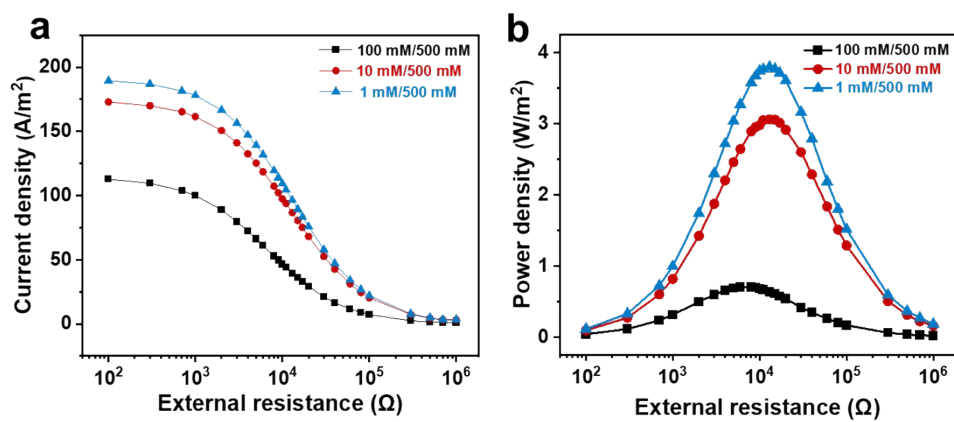


Fig. S14 (a) Current densities and (b) Output power densities of 2D-NFM in NaCl solution with different concentration gradients.

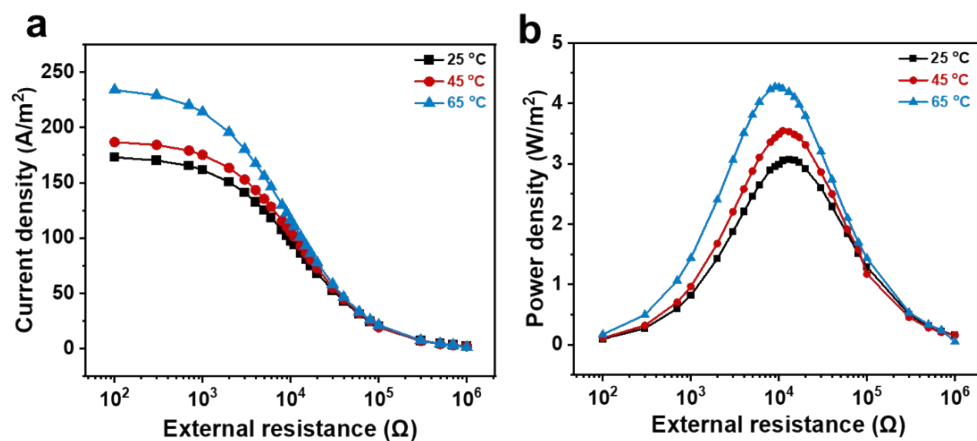


Fig. S15 (a) Current densities and (b) Output power densities of 2D-NFM at different temperatures (0.5 M/0.01 M NaCl).

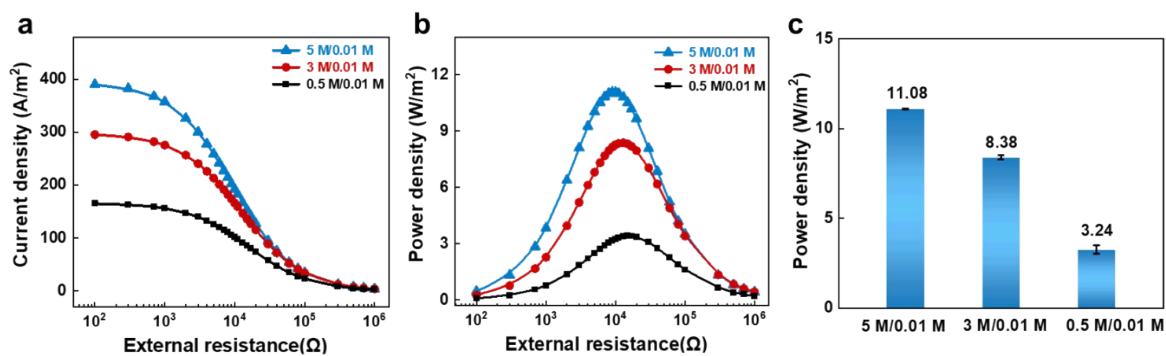


Fig. S16 (a) Current densities and (b, c) Output power densities of 2D-NFM at high salinity solution (0.01 M-0.5/3/5 M NaCl).

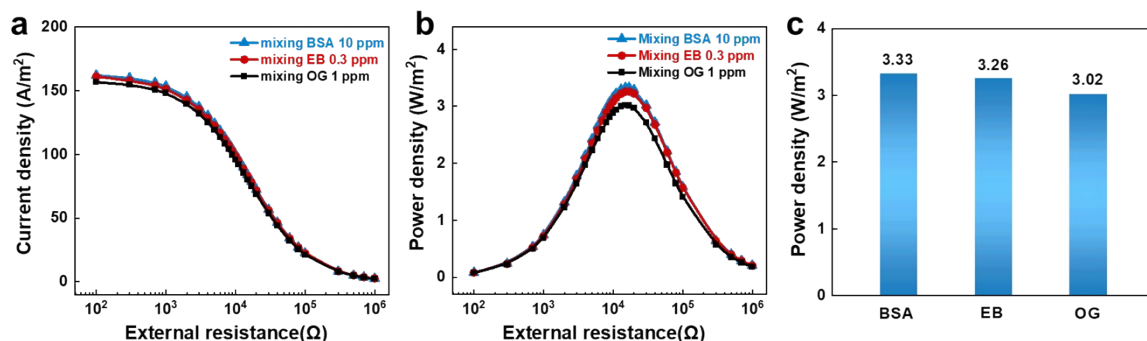


Fig. S17 (a) Current densities and (b, c) Output power densities of 2D-NFM at NaCl solution containing dyes and biological protein (0.01 M/0.5 M NaCl).

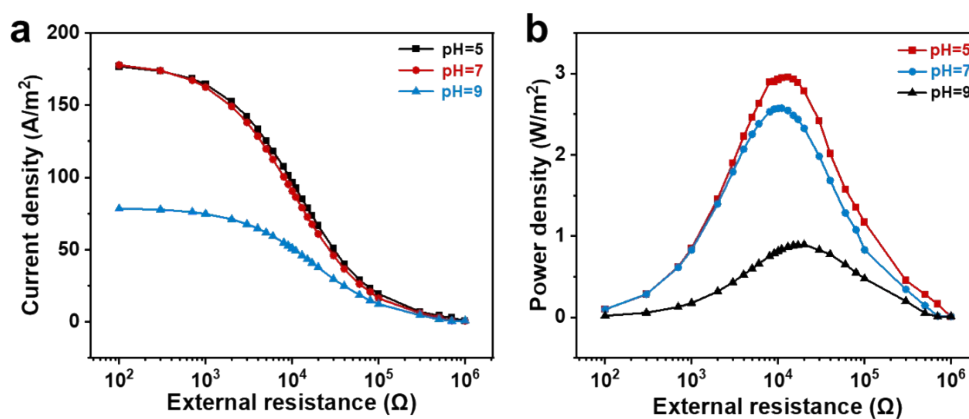


Fig. S18 (a) Current densities and (b) Output power densities of 2D-NFM at different pH (0.5 M/0.01 M NaCl).

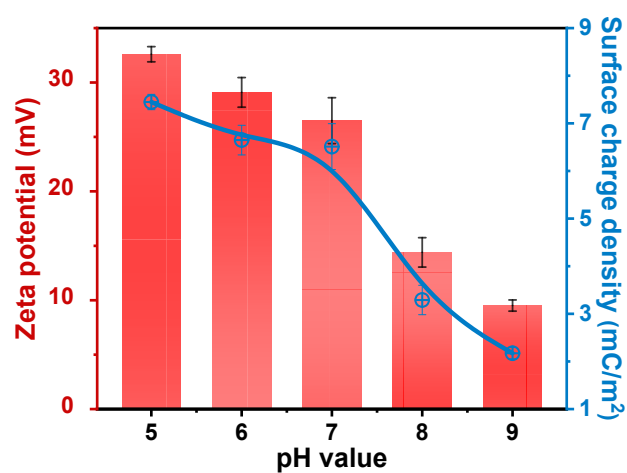


Fig. S19 Zeta potential of 2D-NFM at different pH.

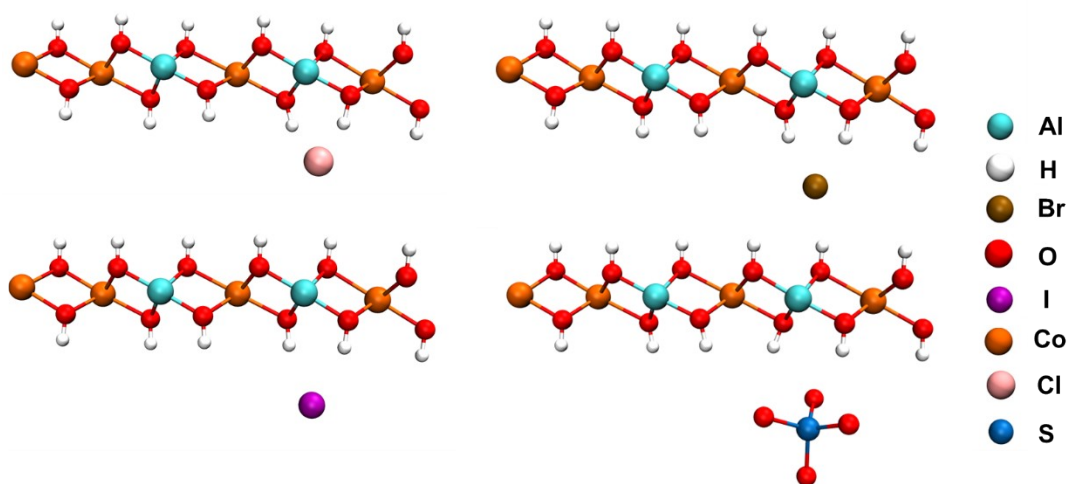


Fig. S20 Models of the interaction between different anions and 2D-NFM.

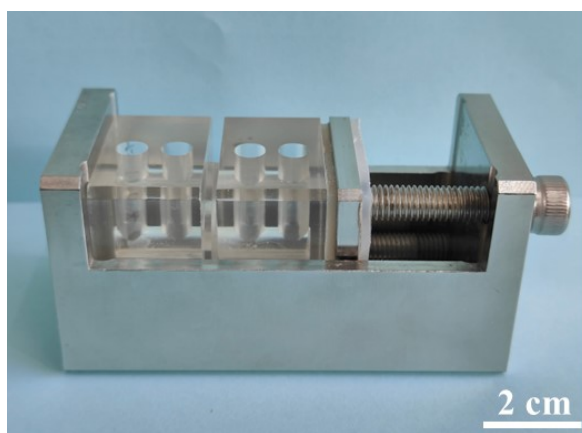


Fig. S21 Photo of osmotic energy harvesting device based on 2D-NFM.

Table S1. Results of ICP-AES analysis of CoAl-CO₃²⁻ LDH.

Element Type	relative atomic mass	Mass concentration (mg/L)	Molar concentration (mol/L)
Al	26.98	0.89	3.3×10 ⁻⁵
Co	58.93	4.73	8.0×10 ⁻⁵

Table S2. Performance comparison of anion-selective membranes.

Membrane	Thickness (μm)	Test area (mm ²)	t.	Power density (W/m ²)	Ref.
P-GO	10.0	0.2	0.65	—	[9]
P-MXene	—	0.2	0.77	—	[10]
MgAl LDH@PBC	7.0	0.02	0.89	0.56	[11]
CoAl LDH	40.0	0.2	—	0.7	[12]
MgAl LDH	11.0	0.05	—	—	[13]
CoAl LDH	20.8	0.2	0.95	—	[14]
P-CMA	23.0	0.65	0.81	0.63	[15]
LDH@AAO	45.8	0.03	—	2.85	[16]
AM-MXene	0.7	180	—	4.2	[17]
P-MF	1000	0.012	0.96	—	[18]
P-ABC	90	180	0.90	0.23	[19]
MgAl LDH	2.6	0.03	—	2.31	[20]
CoAl LDH	16.7	0.03	0.78	3.06	This work

Table S3. The major anion and cation concentrations (M) in seawater.

Ion species	Cl ⁻	SO ₄ ²⁻	Br ⁻	Na ⁺	Mg ²⁺	Ca ²⁺	K ⁺
East Sea	0.475	0.044	0.0005	0.497	0.053	0.010	0.010
South Sea	0.401	0.038	0.0004	0.384	0.052	0.010	0.010

References

- [1] B. Liu, Y. Zhang, Y. Qian, D. Quan, M. Jia, X. Jin, M. Zhou, X. Kong, L. Jiang, *Angew. Chem. Int. Ed.* 63 (2023) e202317361.
- [2] D. Stein, M. Kruithof, C. Dekker, *Phys. Rev. Lett.* 92 (2004) 035901.
- [3] R. Schoch, J. Han, P. Renaud, *Rev. Mod. Phys.* 80 (2008) 839.
- [4] M. Petrowsky, R. Frech, *J. Phys. Chem. B* 113 (2009) 5996-6000.
- [5] W. Xin, Z. Zhang, X. Huang, Y. Hu, T. Zhou, C. Zhu, X. Kong, L. Jiang, L. Wen, *Nat. Commun.* 10 (2019) 3876.
- [6] L. Ding, M. Zheng, D. Xiao, Z. Zhao, J. Xue, S. Zhang, J. Caro, H. Wang, *Angew. Chem. Int. Ed.* 61 (2022) e202206152.
- [7] J. Perdew, K. Burke, M. Ernzerhof, *Phys. Rev. Lett.* 77 (1996) 3865.
- [8] G. Henkelman, B. Uberuaga, H. Jónsson, *J. Chem. Phys.* 113 (2000) 9901-9904.
- [9] J. Ji, Q. Kang, Y. Zhou, Y. Feng, X. Chen, J. Yuan, W. Guo, Y. Wei, L. Jiang, *Adv. Funct. Mater.* 27 (2017) 1603623.
- [10] L. Ding, D. Xiao, Z. Lu, J. Deng, Y. Wei, J. Caro, H. Wang, *Angew. Chem. Int. Ed.* 132 (2020) 8798-8804.
- [11] N. Sheng, M. Zhang, Q. Song, H. Zhang, S. Chen, H. Wang, K. Zhang, *Nano Energy* 101 (2022) 107548.
- [12] T. Konch, T. Dutta, A. Neog, R. Gogoi, K. Raidongia, *J. Phys. Chem. C* 125 (2021) 17939-17949.
- [13] F. Xian, L. Jia, Y. Sugahara, Y. Yamauchi, T. Sasaki, R. Ma, *Chem. Eng. J.* 471 (2023) 144703.
- [14] X. Yu, X. Qian, Q. Wei, Q. Zhang, H. Cheng, W. Ren, *Small* 19 (2023) 2300338.
- [15] J. Shi, X. Sun, Y. Zhang, S. Niu, Z. Wang, Z. Wu, M. An, L. Chen, J. Li, *Carbohydr. Polym.* 327 (2024) 121656.
- [16] Y. Liu, J. Ping, Y. Ying, *Adv. Sci.* 9 (2022) 2103696.
- [17] S. Wang, Z. Wang, Y. Fan, *J. Membr. Sci.* 668 (2023) 121203.
- [18] F. Hashemifar, A. Esfandiar, *J. Mater. Chem. A* 10 (2022) 24915-24926.
- [19] Z. Wu, P. Ji, B. Wang, N. Sheng, M. Zhang, S. Chen, H. Wang, *Nano Energy* 80 (2021) 105554.
- [20] S. Qin, G. Yang, S. Wang, Y. Ma, Z. Wang, L. Wang, D. Liu, W. Lei, *Small* (2024) 2400850.